

Single-molecule magnetism within a family of $[\text{Ln}_2^{\text{III}}\text{Mn}_{10}^{\text{III}}]$ complexes from 2-hydroxymethylpyridine

Rashmi Bagai^a, Wolfgang Wernsdorfer^b, Khalil A. Abboud^a, George Christou^{a,*}

^a Department of Chemistry, University of Florida, Gainesville, FL 32611-7200, USA

^b Institut Néel-CNRS, 38042 Grenoble Cedex 9, France

ARTICLE INFO

Article history:

Received 22 October 2017

Accepted 4 December 2017

Available online 11 December 2017

Keywords:

Manganese

Lanthanides

Clusters

Crystal structure

Single-molecule magnetism

ABSTRACT

A family of heterometallic Ln/Mn (Ln = lanthanide) clusters with a $[\text{Ln}_2^{\text{III}}\text{Mn}_{10}^{\text{III}}]$ core has been synthesized. The complexes $[\text{Ln}_2\text{Mn}_{10}\text{O}_8(\text{O}_2\text{CPh})_{10}(\text{hmp})_6(\text{NO}_3)_4]$ (Ln = Pr (**1**), Nd (**2**), Sm (**3**), Gd (**4**), Tb (**5**), Dy (**6**), Ho (**7**) and Er (**8**)) were prepared from the reaction of $(\text{NBu}_4)[\text{Mn}_4\text{O}_2(\text{O}_2\text{CPh})_9(\text{H}_2\text{O})]$, 2-hydroxymethylpyridine (hmpH) and $\text{Ln}(\text{NO}_3)_3$. The analog with diamagnetic Y^{III} , $[\text{Y}_2\text{Mn}_{10}\text{O}_8(\text{O}_2\text{CPh})_{10}(\text{hmp})_6(\text{NO}_3)_4]$ (**9**), was also synthesized to assist the magnetic studies. Representative complexes **4**, **6** and **9** were characterized by X-ray crystallography, and they contain a layered $[\text{Mn}_{10}\text{O}_8]^{14+}$ core attached at each end to a Ln^{III} or Y^{III} atom. Complexes **5**, **6** and **7** exhibit frequency-dependent out-of-phase (χ_M'') ac susceptibility signals indicating the slow magnetization relaxation of single-molecule magnets (SMMs). Magnetization versus applied dc field hysteresis loops on single crystals of representative complex **6**·3MeCN·MeOH have established it to be a new addition to the family of Mn–Ln SMMs. Relaxation rate versus temperature data for **6** obtained from variable-frequency χ_M'' versus T studies down to 1.8 K were combined with those from dc magnetization decay versus time measurements at lower temperatures, and these were fit to the Arrhenius equation to give an effective barrier to magnetization relaxation (U_{eff}) of 30 K.

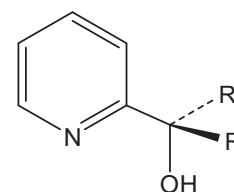
© 2017 Elsevier Ltd. All rights reserved.

1. Introduction

Single-molecule magnets (SMMs) are individual molecules that can function as nanoscale magnetic particles below their blocking temperature (T_B) as a result of the combination of a magnetic moment and magnetoanisotropy of significant magnitudes [1,2]. They thus represent a molecular (or bottom-up) approach to nanoscale magnetic materials, and one that retains all the advantages of molecular chemistry, particularly monodispersity, solubility, crystallinity, and a periphery of organic ligands. Since the initial discovery of the Mn_{12} family of SMMs, the field has expanded to all areas of the periodic table where paramagnetic metal ions are to be found under normal conditions, including both homometallic and heterometallic chemistry, and metal nuclearities from small to very large [1–12]. The recent discovery of a mononuclear Dy SMM that exhibits magnetization hysteresis up to 60 K represents a marvelous breakthrough and the beginning of an important new chapter in the field [13].

At the heart of the health and progress of the SMM field over many years has been the diverse synthetic chemistry that has been brought to bear. A wide range of synthetic methods and ligand

types have been employed, using the molecular advantages mentioned above to crystallize products and characterize them to atomic precision by single-crystal X-ray crystallography. This has been an area in which our own group has been very involved. One approach we have employed widely has been the use of mixed N/O chelate ligands containing one or more alcohol groups,



R = H is hmpH

beginning many years ago in Mn chemistry with 2-(hydroxymethyl)pyridine (hmpH) [14] and related 2,6-bis(hydroxymethyl)pyridine (pdmH₂) [15]. More recently we also introduced modifications to hmpH by replacing the H atoms of the CH₂ arm with Me or Ph groups to explore the effect of increasing bulk near the alkoxide, and a number of very interesting new products were obtained [16,17].

* Corresponding author. Fax: +1 352 392 8757.

E-mail address: christou@chem.ufl.edu (G. Christou).

Of relevance to the present work is the large and growing area of mixed 3d–4f complexes. The breakthrough in 2004 with the report of a Tb₂Cu₂ SMM [18] provided proof-of-feasibility that amalgamation of transition metals with anisotropic Ln^{III} ions could lead to magnetically interesting new molecules and SMMs, and since then this area has expanded greatly first into Mn–Ln chemistry [19,20] and then into many other 3d–4f combinations [11,20–24].

The present work is part of an extension of the use of hmpH (and its bulkier derivatives) into mixed 3d–4f chemistry, specifically with Mn. This sub-area began with the synthesis of the non-carboxylate [Ln₂Mn₂(OH)₂(NO₃)₄(hmp)₄(H₂O)₄](NO₃)₂ family [25] followed by Ln₄Mn₂ [26] and Ln₂Mn₄ [27] carboxylate clusters. More recently, Ln₄Mn₈ and additional Mn₄Ln₂ have been reported [28]. We herein report the development of a synthetic procedure employing hmpH that has yielded a family of Ln₂^{III}Mn₁₀^{II} (1–8) and Y₂^{III}Mn₁₀^{II} (9) complexes. We have obtained the crystal structures of the Gd (4), Dy (6) and Y (9) members, and measured the dc and ac magnetic susceptibilities of all the members of the family, which has also identified some of them to be new SMMs. We shall also describe the results obtained from a single-crystal study of the Dy analog at ultra-low temperatures using a micro-SQUID, which has confirmed the magnetization hysteretic behavior of an SMM.

2. Experimental

2.1. Syntheses

All preparations were performed under aerobic conditions using reagents and solvents as received. (NBu₄)⁺[Mn₄O₂(O₂CPh)₉(H₂O)][−] (10) was prepared as previously described [29].

2.1.1. Preparation of [Pr₂Mn₁₀O₈(O₂CPh)₁₀(hmp)₆(NO₃)₄] (1)

To a stirred red-brown solution of complex 10 (0.36 g, 0.23 mmol) in MeOH/MeCN (1/19 mL) was added Pr(NO₃)₃·5H₂O (0.095 g, 0.23 mmol) followed by hmpH (0.02 mL, 0.23 mmol). The mixture was stirred for another hour, filtered to remove some undissolved solid, and the filtrate layered with Et₂O. Red-brown crystals slowly formed over 7–10 days, and these were collected by filtration, washed with Et₂O, and dried *in vacuo*; the yield was 25%. *Anal. Calc. (Found)* for 1 (C₁₀₆H₈₆N₁₀Mn₁₀O₄₆Pr₂): C, 41.51 (41.55); H, 2.83 (2.84); N, 4.57 (4.38)%. Selected IR data (cm^{−1}): 3434(br), 3063(w), 1707(w), 1606(m), 1566(m), 1403(s), 1290(w), 1176(w) 1069(m), 1051(w), 1027(w), 820(w), 763(w), 718(m), 661(m), 549(m), 429(w).

2.1.2. Preparation of [Nd₂Mn₁₀O₈(O₂CPh)₁₀(hmp)₆(NO₃)₄] (2)

Complex 2 was prepared following the same procedure as for 1 but with Nd(NO₃)₃·6H₂O (0.10 g, 0.23 mmol). The yield was 20%. *Anal. Calc. (Found)* for 2 (C₁₀₆H₈₆N₁₀Mn₁₀O₄₆Nd₂): C, 41.42 (41.77); H, 2.82 (2.88); N, 4.56 (4.76)%. Selected IR data (cm^{−1}): 3446(br), 3063(w), 1698(w), 1607(m), 1566(s), 1473(m), 1401(s), 1315(w), 1291(w), 1175(w), 1157(w), 1069(m), 1050(w), 762(w), 718(m), 660(m), 612(w), 549(m), 460(w), 429(w).

2.1.3. Preparation of [Sm₂Mn₁₀O₈(O₂CPh)₁₀(hmp)₆(NO₃)₄] (3)

Complex 3 was prepared following the same procedure as for 1 but with Sm(NO₃)₃·6H₂O (0.10 g, 0.23 mmol). The yield was 12%. *Anal. Calc. (Found)* for 3 (C₁₀₆H₈₆N₁₀Mn₁₀O₄₆Sm₂): C, 41.26 (41.36); H, 2.81 (2.73); N, 4.54 (4.21)%. Selected IR data (cm^{−1}): 3436(br), 3063(w), 1707(w), 1606(m), 1566(s), 1485(m), 1402(s), 1291(w), 1230(w), 1176(w), 1070(w), 1051(m), 1027(w), 819(w), 765(w), 718(m), 663(m), 614(w), 551(m), 468(w).

2.1.4. Preparation of [Gd₂Mn₁₀O₈(O₂CPh)₁₀(hmp)₆(NO₃)₄] (4)

Complex 4 was prepared following the same procedure as for 1 but with Gd(NO₃)₃·6H₂O (0.10 g, 0.23 mmol). Some crystals were retained in mother liquor for X-ray crystallography, and were characterized as 4·3MeCN·MeOH. The yield was 10%. *Anal. Calc. (Found)* for 4 (C₁₀₆H₈₆Gd₂Mn₁₀N₁₀O₄₆): C, 41.07 (41.35); H, 2.80 (2.81); N, 4.52 (4.22)%. Selected IR data (cm^{−1}): 3456(br), 3063(w), 1710(w), 1607(m), 1566(m), 1485(m), 1384(s), 1292(w), 1230(w), 1175(w), 1070(w), 1051(m), 1027(w), 841(w), 763(w), 718(m), 662(m), 616(w), 552(m), 464(w).

2.1.5. Preparation of [Tb₂Mn₁₀O₈(O₂CPh)₁₀(hmp)₆(NO₃)₄] (5)

Complex 5 was prepared following the same procedure as for 1 but with Tb(NO₃)₃·5H₂O (0.10 g, 0.23 mmol). The yield was 20%. *Anal. Calc. (Found)* for 5 (C₁₀₆H₈₆N₁₀Mn₁₀O₄₆Tb₂): C, 41.03 (41.03); H, 2.79 (2.80); N, 4.51 (4.31)%. Selected IR data (cm^{−1}): 3432(br), 3062(w), 1710(w), 1605(m), 1566(s), 1487(m), 1401(s), 1291(w), 1175(w), 1157(w), 1070(m), 1051(w), 1026(w), 818(w), 765(w), 718(m), 665(m), 616(w), 550(m), 465(w).

2.1.6. Preparation of [Dy₂Mn₁₀O₈(O₂CPh)₁₀(hmp)₆(NO₃)₄] (6)

Complex 6 was prepared following the same procedure as for 1 but with Dy(NO₃)₃·5H₂O (0.10 g, 0.23 mmol). Some crystals were retained in mother liquor for X-ray crystallography, and were characterized as 6·3MeCN·MeOH. The yield was 15%. *Anal. Calc. (Found)* for 6 (C₁₀₆H₈₆Dy₂Mn₁₀N₁₀O₄₆): C, 40.93 (40.50); H, 2.79 (2.90); N, 4.50 (4.24)%. Selected IR data (cm^{−1}): 2961(s), 2928(m), 2871(w), 1580(s), 1551(s), 1484(vs), 1421(vs), 1376(m), 1228(m), 1090(w), 906(w), 787(w), 663(w), 602(m), 508(w), 438(m).

2.1.7. Preparation of [Ho₂Mn₁₀O₈(O₂CPh)₁₀(hmp)₆(NO₃)₄] (7)

Complex 7 was prepared following the same procedure as for 1 but with Ho(NO₃)₃·5H₂O (0.10 g, 0.23 mmol). The yield was 15%. *Anal. Calc. (Found)* for 7·2H₂O (C₁₀₆H₉₀N₁₀Mn₁₀O₄₈Ho₂): C, 40.40 (40.11); H, 2.88 (2.79); N, 4.44 (4.23)%. Selected IR data (cm^{−1}): 3432(br), 3063(w), 1602(m), 1565(s), 1488(m), 1385(s), 1309(w), 1175(w), 1157(w), 1069(m), 1051(w), 1025(w), 765(w), 718(m), 670(m), 547(m), 466(w).

2.1.8. Preparation of [Er₂Mn₁₀O₈(O₂CPh)₁₀(hmp)₆(NO₃)₄] (8)

Complex 8 was prepared following the same procedure as for 1 but with Er(NO₃)₃·5H₂O (0.10 g, 0.23 mmol). The yield was 10%. *Anal. Calc. (Found)* for 8·3H₂O (C₁₀₆H₉₂N₁₀Mn₁₀O₄₈Er₂): C, 40.11 (39.85); H, 2.92 (2.84); N, 4.41 (4.23)%. Selected IR data (cm^{−1}): 3430(br), 3063(w), 1709(w), 1603(m), 1565(s), 1488(m), 1400(s), 1306(w), 1175(w), 1157(w), 1070(m), 1051(w), 1027(w), 817(w), 765(w), 717(m), 673(m), 612(w), 549(m).

2.1.9. Preparation of [Y₂Mn₁₀O₈(O₂CPh)₁₀(hmp)₆(NO₃)₄] (9)

Complex 9 was prepared following the same procedure as for 1 but with Y(NO₃)₃·6H₂O (0.087 g, 0.23 mmol). Some crystals were retained in mother liquor for X-ray crystallography, and were characterized as 9·4MeCN. The yield was 15%. *Anal. Calc. (Found)* for 9 (C₁₀₆H₈₆N₁₀Mn₁₀O₄₆Y₂): C, 42.97 (42.69); H, 2.92 (2.83); N, 4.73 (5.17)%. Selected IR data (cm^{−1}): 3421(br), 3063(w), 1698(w), 1602(m), 1564(s), 1506(m), 1385(s), 1311(w), 1176(w), 1069(m), 1051(w), 765(w), 718(m), 667(m), 547(w), 467(w).

2.2. X-ray crystallography

Data were collected on a Siemens SMART PLATFORM equipped with a CCD area detector and a graphite monochromator utilizing Mo K α radiation (λ = 0.71073 Å). Suitable crystals were attached to glass fibers using silicone grease and transferred to a goniostat where they were cooled to 173 K for data collection. Cell parameters were refined using 8192 reflections. A full sphere of data (1850

frames) was collected using the ω -scan method (0.3° frame width). The first 50 frames were re-measured at the end of the data collection to monitor instrument and crystal stability (maximum correction on I was <1%). Absorption corrections by integration were applied based on measured indexed crystal faces. The structure was solved by the direct methods in *SHELXTL2014* [30] and refined on F^2 using full-matrix least-squares. The non-H atoms were treated anisotropically, whereas the H atoms were placed in calculated, ideal positions and refined as riding on their respective C atoms.

For **4**·3MeCN·MeOH and **6**·3MeCN·MeOH, the asymmetric unit consists of $\frac{1}{2}$ the $\text{Mn}_{10}\text{Gd}_2$ or $\text{Mn}_{10}\text{Dy}_2$ cluster, a disordered MeCN in a general position, and $\frac{1}{2}$ MeCN disordered against a $\frac{1}{2}$ MeOH molecule about an inversion center. A total of 825 (**4**) or 817 (**6**) parameters were refined in the final cycle of refinement using 20616 (**4**) or 10817 (**6**) reflections with $I > 2\sigma(I)$ to give $R_1(wR_2)$ of 6.43(17.13)% and 5.08(13.30)% for **4** and **6**, respectively.

For **9**·4MeCN, the asymmetric unit consists of $\frac{1}{2}$ the Mn_{10}Y_2 cluster and two MeCN molecules. The latter are disordered and could not be modeled properly, thus program *SQUEEZE* [31], a part of the *PLATON* package of crystallographic software [32], was used to calculate the solvent disorder area and remove its contribution to the overall intensity data. A total of 778 parameters were refined in the final cycle of refinement using 6197 reflections with $I > 2\sigma(I)$ to yield $R_1(wR_2)$ of 7.10(16.14)%, respectively.

Unit cell data and structure refinement details for the complexes are listed in Table 1.

2.3. Other studies

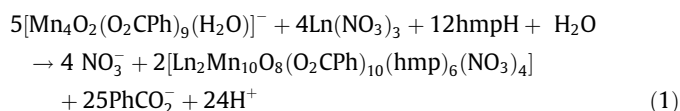
Infrared spectra were recorded in the solid state (KBr pellets) on a Nicolet Nexus 670 FTIR spectrometer in the 400–4000 cm^{-1} range. Elemental analyses (C, H, N) were performed by the in-house facilities of the University of Florida, Chemistry Department. Variable-temperature dc and ac magnetic susceptibility data were collected at the University of Florida using a Quantum Design MPMS-XL SQUID susceptometer equipped with a 7 T magnet and operating in the 1.8–300 K range. Samples were embedded in solid eicosane to prevent torquing. Pascal's constants were used to estimate the diamagnetic correction, which was subtracted from the experimental susceptibility to give the molar paramagnetic susceptibility (χ_M). Studies at ultra-low temperatures (<1.8 K) were performed on single crystals at Grenoble using an array of micro-

SQUIDs [33]. The high sensitivity of this magnetometer allows the study of single crystals of the order of 10–500 μm ; the field can be applied in any direction by separately driving three orthogonal coils.

3. Results and discussion

3.1. Syntheses

One common synthetic procedure to high-nuclearity Mn^{III} -containing clusters that we and others have employed on numerous occasions in the past has involved the reaction of a chelate with preformed $[\text{Mn}_3^{\text{III}}\text{O}(\text{O}_2\text{CR})_6\text{L}_3]^+$ triangular complexes [34–37]. The chelate has the dual function of encouraging molecular products rather than polymers, and fostering high-nuclearity products if good binding groups such as alkoxides are present. In the present work, another complex was employed that had also proven to be a good stepping-stone to high nuclearity products, namely $(\text{NBu}_4)[\text{Mn}_4^{\text{III}}\text{O}_2(\text{O}_2\text{CPh})_9(\text{H}_2\text{O})]$ (**10**) [29]. Reaction of **10** with 1 equiv each of hmpH and $\text{Ln}(\text{NO}_3)_3$ or $\text{Y}(\text{NO}_3)_3$ in MeCN/MeOH led to subsequent isolation of red-brown crystals of complexes **1–9** in fair yields of 10–30%. Attempts to increase yields by layering with Et_2O gave more product but contaminated with white solids, so we were happy to settle for lower yields of pure product. The reaction is summarized in Eq. (1).



We tried to make the complete Ln series (except Pm), but the later lanthanides Tm, Yb and Lu gave products that were clearly not isostructural with **1–8**, and we assume this is related to their smaller size. We were also unable to get the Eu analog pure. Similarly for the Ce reaction, for reasons we assume involve redox reactions – we have seen elsewhere on multiple occasions that the Ce^{IV} oxidation state is favored in mixed-metal Mn–Ce chemistry involving high oxidation state $\text{Mn}^{\text{III}}/\text{Mn}^{\text{IV}}$ [38].

The reactions were sensitive to the $\text{Mn}_4\text{:hmpH}:\text{Ln}^{\text{III}}$ ratio. Other ratios gave poor crystallinity and/or mixtures of products. The mixed MeCN:MeOH solvent system was also important to give clean products **1–9**. The structures of representative Ln^{III} complexes **4** and **6**, and the Y^{III} complex **9**, were determined by X-ray

Table 1
Crystallographic and structure refinement data for **4**, **6** and **9**.

	4	6	9
Formula ^{a,b}	$\text{C}_{113}\text{H}_{99}\text{Gd}_2\text{Mn}_{10}\text{N}_{13}\text{O}_{47}$	$\text{C}_{113}\text{H}_{99}\text{Dy}_2\text{Mn}_{10}\text{N}_{13}\text{O}_{47}$	$\text{C}_{114}\text{H}_{98}\text{Mn}_{10}\text{N}_{14}\text{O}_{46}\text{Y}_2$
FW (g/mol) ^b	3254.97	3265.46	3127.28
Space group	$P\bar{1}$	$P\bar{1}$	$P\bar{1}$
a (Å)	14.7083(7)	14.7358(11)	14.737(3)
b (Å)	15.2173(7)	15.2150(12)	15.080(3)
c (Å)	16.7604(8)	16.6441(13)	16.569(3)
α (°)	67.414(1)	67.629(1)	67.175(4)
β (°)	65.549(1)	65.658(1)	65.668(4)
γ (°)	87.627(1)	87.636(1)	87.374(4)
V (Å ³)	3122.0(3)	3114.3(4)	3063.9(10)
Z	1	1	1
T (K)	173(2)	173(2)	173(2)
λ (Å) ^b	0.71073	0.71073	0.71073
ρ_{calc} (g/cm ³)	1.731	1.733	1.733
μ (mm ⁻¹)	2.112	2.252	2.024
R_1 ^{c,d}	0.0643	0.0508	0.0742
wR_2 ^e	0.1779	0.1334	0.1635

^a **4**·3MeCN·MeOH, **6**·3MeCN·MeOH, and **9**·4MeCN.

^b Including solvent molecules.

^c $I > 2\sigma(I)$.

^d $R_1 = \sum(|F_o| - |F_c|)/\sum|F_o|$.

^e $wR_2 = [\sum(w(F_o^2 - F_c^2)^2)/\sum(w(F_o^2)^2)]^{1/2}$.

crystallography; all the complexes gave essentially superimposable IR spectra, and elemental analyses in agreement with the given formulations. The compounds are air stable, but interstitial solvent molecules are easily lost during vacuum drying and the solids are slightly hygroscopic.

3.2. Description of structures

The labeled structure of representative complex **4** is shown in Fig. 1, and selected interatomic distances and angles for the cores of **4**, **6** and **9** are compared in Table 2. They all crystallize in triclinic space group $P\bar{1}$ with the $\text{Ln}_2\text{Mn}_{10}$ molecules lying on inversion centers, and their structures are essentially identical except for the identity of the Ln^{III} or Y^{III} atoms (Fig. S1, Supplementary Information), and only the structure of **4** is described here. The complex contains a $[\text{Gd}_2\text{Mn}_{10}(\mu_3\text{-O}^{2-})_4(\mu_4\text{-O}^{2-})_4]^{20+}$ core consisting of five layers of three types with an ABCBA arrangement (Fig. 2). Layer A is the Gd atom, layer B is a triangular Mn_3^{II} unit (Mn1, Mn2, Mn3), and layer C is a Mn_4^{II} rhombus (Mn4, Mn4', Mn5, Mn5'). Each layer is held together and linked to its neighboring layers by a combination of four $\mu_3\text{-O}^{2-}$ and four $\mu_4\text{-O}^{2-}$ ions (the O^{2-} are O1–O4 and their symmetry partners) and ten benzoate groups, six of which are in $\eta^1:\eta^1:\mu$ -bridging modes and four are in $\eta^2:\eta^1:\mu_3$ -bridging modes (Scheme 1). Peripheral ligation is provided by four η^2 -chelating NO_3^-

Table 2
Selected metric parameters (\AA , $^\circ$) for **4**, **6**, and **9**.

	4 (Gd)	6 (Dy)	9 (Y)
Ln–O1	2.510(4)	2.478(3)	2.451(4)
Ln–O11	2.325(5)	2.315(4)	2.291(5)
Ln–O12	2.360(5)	2.341(4)	2.334(5)
Ln–O13	2.312(5)	2.301(4)	2.294(6)
Mn2–O1	1.944(4)	1.953(3)	1.944(5)
Mn2–O4	1.841(4)	1.842(3)	1.845(4)
Mn3–O1	1.916(4)	1.911(3)	1.911(4)
Mn3–O2	1.883(4)	1.878(3)	1.869(4)
Mn3–O12	1.905(4)	1.904(3)	1.892(4)
Mn4–O2	1.912(4)	1.919(3)	1.917(4)
Mn4–O3'	1.947(4)	1.949(3)	1.960(4)
Mn4–O4 ^a	2.125(4)	2.117(3)	2.078(4)
Mn5–O2	1.907(4)	1.905(3)	1.909(4)
Mn5–O3'	1.939(4)	1.939(3)	1.933(5)
Mn5–O3 ^a	2.477(4)	2.465(3)	2.440(4)
Mn5–O4'	1.884(4)	1.887(3)	1.896(4)
Mn3–O1–Mn1	133.2(2)	132.95(18)	132.8(3)
Mn3–O1–Mn2	108.5(2)	108.24(17)	107.8(3)
Mn1–O1–Mn2	106.35(19)	106.13(15)	105.78(19)
Ln1–O11–Mn1	110.4(2)	110.13(19)	110.5(3)
Ln1–O12–Mn3	107.35(19)	107.19(14)	107.21(18)
Ln1–O13–Mn2	107.8(2)	108.12(17)	108.0(2)

^a JT-elongated Mn–O²⁻ bond.

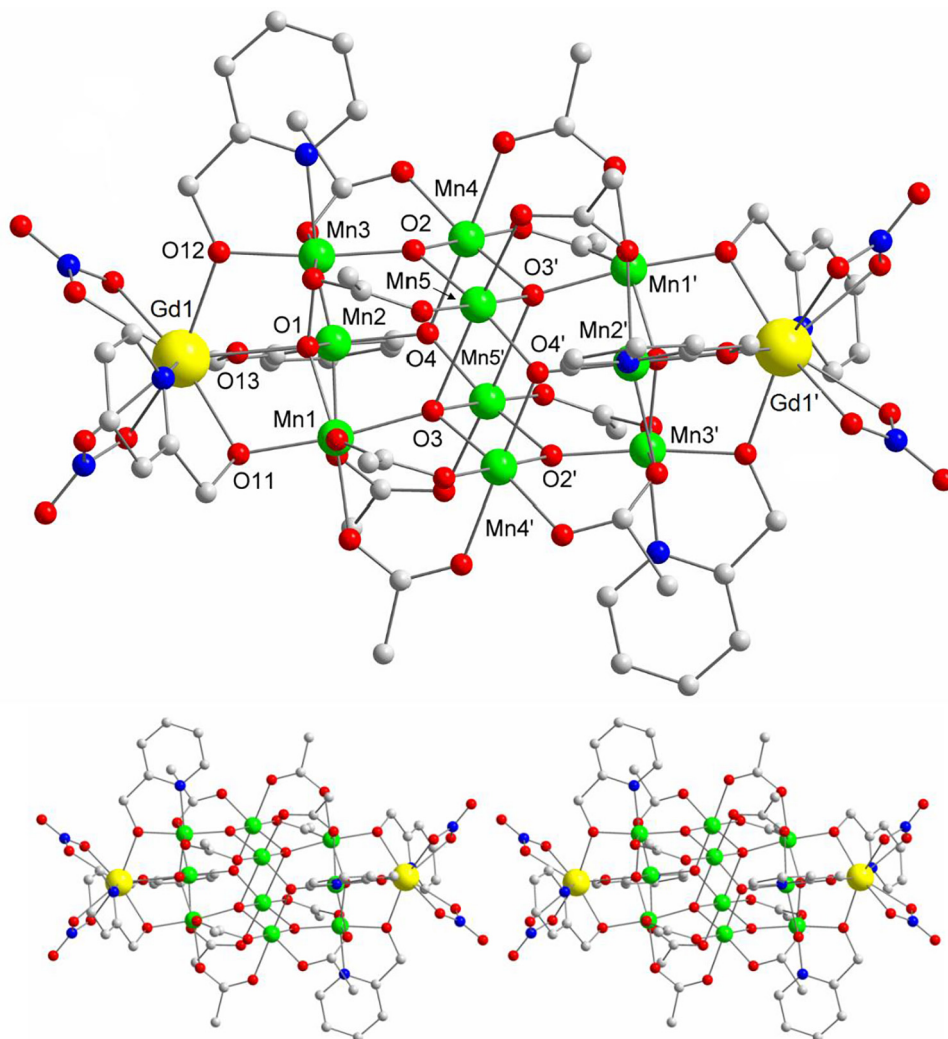


Fig. 1. Labeled structure and stereo-pair for complex **4**, with H atoms and phenyl rings (except for the *ipso* C atoms) omitted for clarity. Color code: Gd, yellow; Mn, green; O, red; N, blue; C, gray. (Color online.)

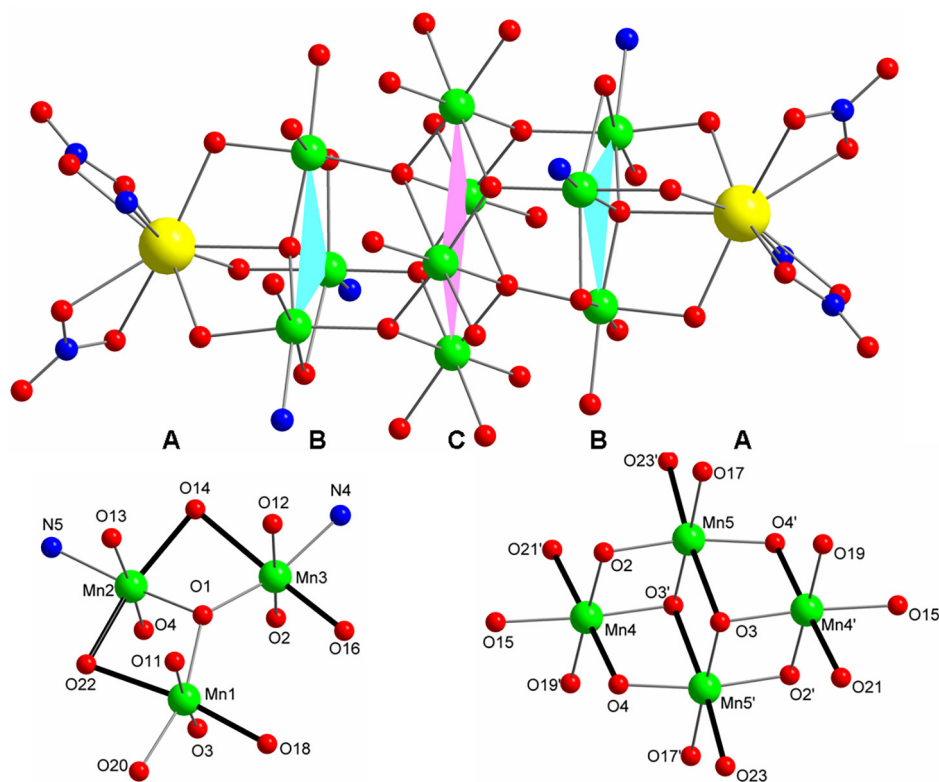
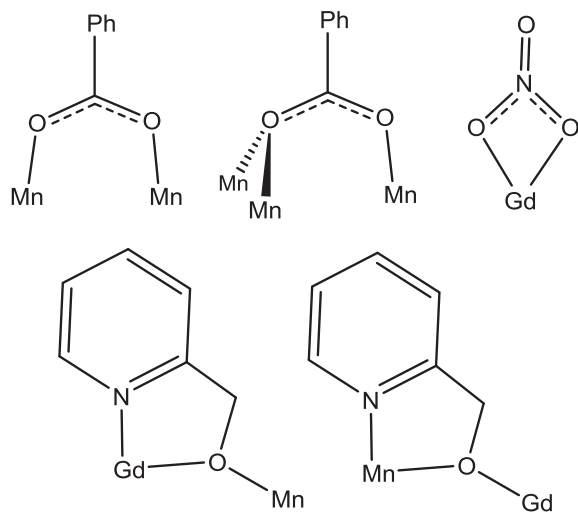


Fig. 2. (top) Centrosymmetric core of **4** emphasizing the ABCBA layer structure. (bottom) The **B** (left) and **C** (right) layers showing the JT elongation axes as thicker black bonds. Color code: Gd, yellow; Mn, green; O, red; N, blue; C, gray. (Color online.)



Scheme 1.

groups, two on each Gd atom, and six $\eta^2:\eta^1:\mu_2$ -chelating hmp[−] groups, one each on the Gd1 atoms, and Mn2, Mn2', Mn3 and Mn3' of layer **B**; the hmp[−] alkoxide arms bridge Gd atoms with Mn atoms of layer **B**, or vice versa (Scheme 1). The Mn and Gd atoms are six- and nine-coordinate, respectively, and the Mn^{III} oxidation states were determined using a combination of charge-balance considerations, inspection of metric parameters, and bond valence sum (BVS) calculations [39]; the latter for **4** are listed in Table 3, and for the others in Table S1.

As expected, the near-octahedral Mn^{III} centers exhibit a Jahn–Teller (JT) distortion, taking the usual form of an axial elongation.

Table 3
BVS Values for the Mn atoms of 4·3MeCN·MeOH.^a

Atom	Mn ^{II}	Mn ^{III}	Mn ^{IV}
Mn1	3.09	<u>2.83</u>	2.97
Mn2	3.33	<u>3.08</u>	3.18
Mn3	3.31	<u>3.06</u>	3.16
Mn4	3.15	<u>2.88</u>	3.03
Mn5	3.06	<u>2.80</u>	2.94

^a The underlined value is the one closest to the charge for which it was calculated. The oxidation state of a particular atom is the nearest whole number to the underlined value.

The Mn^{III} JT axes of layer **C** are approximately parallel to each other (thicker black bonds in Fig. 2, bottom right), whereas two of those in layer **B** are parallel (on Mn1 and Mn3) but the third (Mn2) is near-perpendicular to them (Fig. 2, bottom left). All atoms on JT axes are O atoms, and in layer **B** they are all from carboxylate groups, a common situation since JT axes avoid, if possible, the shorter, stronger Mn–O^{2−} bonds. However, in layer **C**, this cannot be avoided, and all four JT axes have one O^{2−} ion and one carboxylate O atom. As a result, these JT Mn–O^{2−} bonds Mn4–O4 (2.125(4) Å), Mn5–O3 (2.476(4) Å), and their symmetry partners, are much longer than the others (1.841(4)–1.947(4) Å). Also long is the Gd– μ_4 -O^{2−} bond (Gd–O1 = 2.509(4) Å). The same situations re JT axes and long Ln(Y)–O^{2−} bonds are found in **6** and **9** (Table 2).

The overall structure of these Mn₁₀Ln₂ complexes is unprecedented in 3d–4f chemistry, but the central BCB Mn₁₀ unit is somewhat similar to that in the homometallic complexes [Mn₁₀O₈(O₂CPh)₆L₈], where L is the anion of picolinic acid (**11**) or dibenzoylmethane (**12**) [40]. **11** and **12** also contain two Mn₃ triangular units above and below a central Mn₄ planar unit; however, there are significant differences in the exact disposition of the

three units and in the resulting metric parameters. There is also one other $\text{Ln}_2\text{Mn}_{12}$ cluster in the literature, but this has a completely different core structure to **4** [41].

3.3. Magnetochemistry

Solid-state, variable-temperature dc magnetic susceptibility data were collected on powdered microcrystalline samples of complexes **1–9** in the 5.0–300 K range and in a 0.1 T magnetic field (Fig. 3). We will first discuss the data for $[\text{Y}_2\text{Mn}_{10}]$ (**9**) and $[\text{Gd}_2\text{Mn}_{10}]$ (**4**): the first will allow characterization of the magnetic properties of the Mn_{10} sub-unit alone, and the second will show the resultant of its exchange coupling with isotropic Gd^{3+} ions ($S = 7/2$, $^8\text{S}_{7/2}$ free-ion term). These will assist the interpretation of the data for the other complexes.

3.3.1. Complexes **9** (Y_2Mn_{10}) and **4** ($\text{Gd}_2\text{Mn}_{10}$)

For **9**, the value of $\chi_{\text{M}}T$ smoothly decreases from $28.4 \text{ cm}^3 \text{ Kmol}^{-1}$ at 300 K to $10.7 \text{ cm}^3 \text{ Kmol}^{-1}$ at 5 K (Fig. 3). The 300 K value is slightly less than the spin-only ($g = 2$) value of $30.0 \text{ cm}^3 \text{ Kmol}^{-1}$ for ten non-interacting Mn^{III} ions, and decreases with decreasing temperature indicating the presence of dominant intramolecular antiferromagnetic (AF) exchange interactions. For **4**, the value of $\chi_{\text{M}}T$ decreases from $37.9 \text{ cm}^3 \text{ Kmol}^{-1}$ at 300 K to $32.4 \text{ cm}^3 \text{ Kmol}^{-1}$ at 50 K, stays roughly constant down to 15 K, and then decreases rapidly to $27.4 \text{ cm}^3 \text{ Kmol}^{-1}$ at 5.0 K. The 300 K value is less than the spin-only value of $45.7 \text{ cm}^3 \text{ Kmol}^{-1}$ for ten Mn^{III} and two Gd^{III} non-interacting ions.

To estimate the ground state spin of **9**, magnetization (M) data were collected at various fields up to 7 T and in the 1.8–10 K temperature range. Attempts were made to fit the data, using the program MAGNET [42], by diagonalizing the spin Hamiltonian matrix assuming only the ground state is populated, incorporating axial anisotropy ($D\hat{S}_z^2$) and Zeeman terms, and employing a full powder average. The spin Hamiltonian is given by Eq. (2), where S_z

$$\mathcal{H} = D\hat{S}_z^2 + g\mu_{\text{B}}\mu_0\hat{S} \cdot H \quad (2)$$

is the z-axis spin operator, g is the electronic g factor, μ_0 is the vacuum permeability, and H is the applied field; the last term in Eq. (2) is the Zeeman energy associated with the applied magnetic field. As is often the case for a high nuclearity cluster, no acceptable fit could be obtained using all the data, due to a high density of low-lying

excited states as a result of weak interactions and/or spin frustration effects; field-induced stabilization of excited state terms and even crossing with ground state terms leads to their population and a resulting increase in the magnetization. We thus progressively removed data at higher fields, and a fair fit was obtained using only data at weak applied fields (0.1–0.8 T). These data, plotted as reduced magnetization ($M/N\mu_{\text{B}}$) versus H/T (N is Avogadro's number and μ_{B} is the Bohr magneton) are shown in Fig. 4, and the obtained fit (solid lines) gave $S = 4$, $g = 2.01(2)$ and $D = -0.9$ (1 cm^{-1}). Alternative fits with $S = 3$ or 5 gave unreasonable values of g of 2.67 and 1.65, respectively, and were rejected. The precision of the g and D values were estimated from the root-mean-square D versus g error surface generated for the fit for **9** using the program GRID [43] and shown as a 2-D contour surface (Fig. S2); it shows a very soft minimum consistent with the small range of data employed. The accuracy of the obtained D value is likely poor; even using just weak field data probably does not avoid all complications from low-lying excited states, and contributions from the latter to the non-superimposability of the isofield data in Fig. 4 will be reflected in the fit by a larger D value. The fit value should therefore be taken as a rough upper limit, the true D value likely being significantly smaller. For $\text{Mn}_{10}\text{Gd}_2$ complex **4**, no acceptable fit of dc $M/N\mu_{\text{B}}$ versus H/T data could be obtained, consistent with the expected weak exchange interactions between the Mn_{10} unit and Gd^{III} ions (vide infra) and thus increased complications from low-lying excited states.

For an independent check on the ground state, ac susceptibility data for **9** were collected in the 1.8–15 K range under a 3.5 G ac field oscillating at frequencies in the 50–1000 Hz range. The in-phase (χ'_{M}) signals, plotted as $\chi'_{\text{M}}T$ versus T in Fig. 5, provide an alternative means to determine the ground state that precludes complications from a dc field [44]. $\chi'_{\text{M}}T$ steadily decreases with decreasing T , consistent with depopulation of low-lying excited states. Extrapolating the data from above 4 K (to avoid the faster decrease at lower T that is likely due to weak intermolecular interactions and zfs) gives just under $10 \text{ cm}^3 \text{ Kmol}^{-1}$ at 0 K, indicating an $S = 4$ ground state and $g < 2$ slightly, as expected for Mn^{III} systems; the spin-only $\chi'_{\text{M}}T$ for $S = 3$ and 5 is 6.0 and $15.0 \text{ cm}^3 \text{ Kmol}^{-1}$, respectively.

The in-phase $\chi'_{\text{M}}T$ for **4** (Fig. 5) steadily decreases with decreasing T , and then below ~ 6 K decreases more rapidly. Interestingly, the $\chi'_{\text{M}}T$ in the 8–15 K range is approximately the $\chi'_{\text{M}}T$ of **9** plus that for two non-interacting Gd^{III} , i.e., the plots of **4** and **9** are

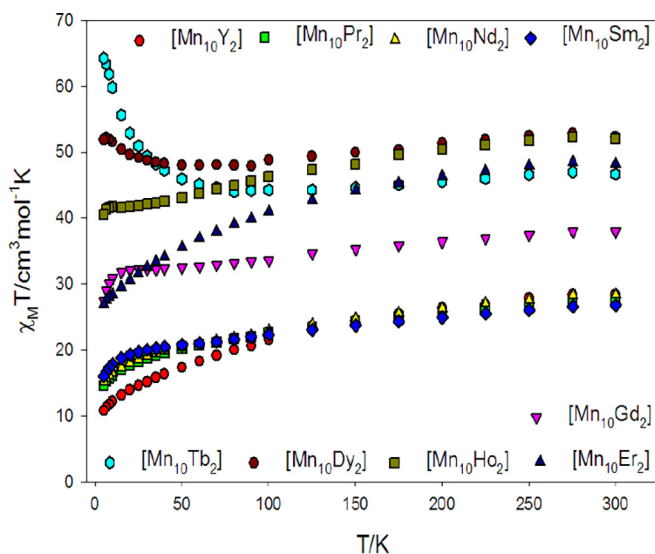


Fig. 3. $\chi_{\text{M}}T$ vs. T plots for complexes **1–9** in a 0.1 T (1000 G) applied dc field.

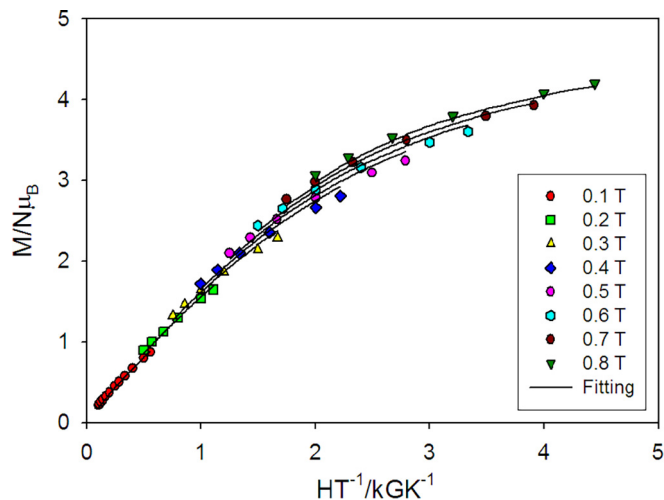


Fig. 4. Plot of reduced magnetization ($M/N\mu_{\text{B}}$) vs. H/T for **9**. See the text for the fit parameters.

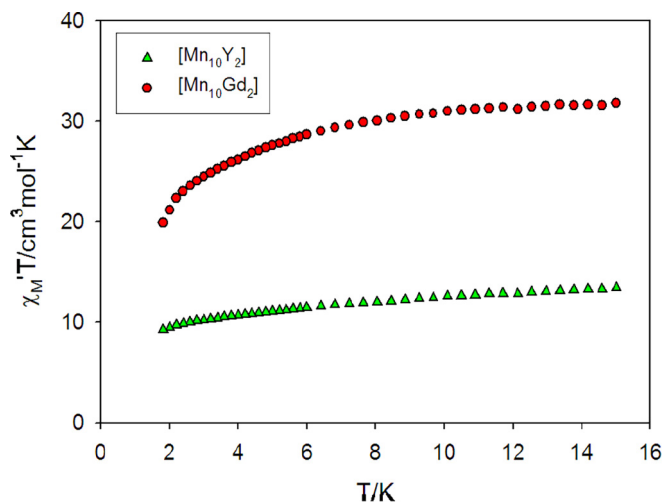


Fig. 5. Ac in-phase $\chi'_M T$ vs. T plots for **4** ($\text{Mn}_{10}\text{Gd}_2$) and **9** (Mn_{10}Y_2) in the 1.9–15.0 K range.

nearly parallel; $\chi'_M T$ for a Gd^{III} is essentially T -independent at $\sim 8 \text{ cm}^3 \text{ Kmol}^{-1}$, as seen for $\text{Gd}(\text{NO}_3)_3 \cdot 6\text{H}_2\text{O}$ (Fig. S3). We thus feel a reasonable description is that $\chi'_M T$ for **4** above 8 K represents the sum of the Mn_8 sub-unit plus those of two essentially uncoupled Gd^{III} . Below $\sim 8 \text{ K}$, weak $\text{Gd} \cdots \text{Mn}$ interactions begin to become significant and $\chi'_M T$ decreases. Note that weak $\text{Gd} \cdots \text{Mn}$ interactions are expected from the structure, since there is only one bridging O^{2-} ion, the usually dominant superexchange pathway in $\text{M}/\text{O}/\text{RCO}_2^-$ clusters, and even that is μ_4 and thus gives a long $\text{Gd}-\text{O}$ bond (vide supra). Not only will the J_{GdMn} be weak, spin frustration effects will be operative in the GdMn_2 triangles [45] if the J_{MnMn} between the layer **B** Mn^{III} are weakly **AF**, as they most likely are, regardless of whether the J_{GdMn} are **AF** or **F**. As a result, it is extremely likely that the Gd spin vectors will be in intermediate orientations (m_x states), and this would rationalize the ac plot showing (i) very low-lying excited states (the plot is steeply dropping with decreasing T) due to weak J_{GdMn} ; and (ii) a ground state not that different from the $S = 4$ of **9**.

The out-of-phase (χ''_M) plots for **4** and **9** (Fig. S5) show only weak tails of frequency-dependent signals below 1.8 K, the operating minimum of our SQUID. The signals for **4** are stronger than those for **9**, but still very weak – it could be due to small changes to either the ground state S or to perturbation of the magnetic properties of the Mn_{10} subunit on Gd -for- Y substitution, or both.

3.3.2. Complexes **1** ($\text{Pr}_2\text{Mn}_{10}$), **2** ($\text{Nd}_2\text{Mn}_{10}$), **3** ($\text{Sm}_2\text{Mn}_{10}$)

For these three complexes with anisotropic early lanthanides, the $\chi_M T$ versus T plots were similar (Fig. 3). The $\chi_M T$ at 300 K is 27.4, 28.4, and 26.8 $\text{cm}^3 \text{ Kmol}^{-1}$ for **1**, **2** and **3**, respectively. In each case, $\chi_M T$ then decreases with decreasing temperature to 14.6, 15.2, and 16.0 $\text{cm}^3 \text{ Kmol}^{-1}$, respectively, at 5.0 K. The $\chi_M T$ versus T behaviors of **1–3** are thus essentially parallel to that of **9**, except at the lowest temperatures. They also give exhibit very weak χ''_M signals like those of **9**.

3.3.3. Complexes **5** ($\text{Tb}_2\text{Mn}_{10}$), **6** ($\text{Dy}_2\text{Mn}_{10}$), **7** ($\text{Ho}_2\text{Mn}_{10}$), and **8** ($\text{Er}_2\text{Mn}_{10}$)

The $\chi_M T$ for **5** decreases from 46.7 $\text{cm}^3 \text{ Kmol}^{-1}$ at 300 K to a minimum at 80 K and then increases to 64.3 $\text{cm}^3 \text{ Kmol}^{-1}$ at 5.0 K (Fig. 3). The $\chi_M T$ for **6** ($\text{Mn}_{10}\text{Dy}_2$) decreases slightly from 52.3 $\text{cm}^3 \text{ Kmol}^{-1}$ at 300 K to 48.0 $\text{cm}^3 \text{ Kmol}^{-1}$ at 50 K and then increases to 51.9 $\text{cm}^3 \text{ Kmol}^{-1}$ at 5.0 K. The $\chi_M T$ for **7** and **8** decrease from 51.9 and 49.5 $\text{cm}^3 \text{ Kmol}^{-1}$ at 300 K to 40.5 and 21.3 $\text{cm}^3 \text{ Kmol}^{-1}$ at 5.0 K, respectively (Fig. 3). The **AF** interactions within

the Mn_{10} unit make all 300 K values less than the spin-only value of 53.6, 58.3, 58.1 and 52.9 $\text{cm}^3 \text{ Kmol}^{-1}$ for ten Mn^{III} ions and two Tb^{III} ($4f^8$, 7F_6 , 23.6 $\text{cm}^3 \text{ Kmol}^{-1}$), two Dy^{III} ($4f^9$, ${}^6H_{15/2}$, 28.3 $\text{cm}^3 \text{ Kmol}^{-1}$), two Ho^{III} ($4f^{10}$, 5I_8 , 28.1 $\text{cm}^3 \text{ Kmol}^{-1}$) and two Er^{III} ($4f^{11}$, ${}^4I_{15/2}$, 22.9 $\text{cm}^3 \text{ Kmol}^{-1}$) non-interacting ions. M versus applied field (H) plots at 1.8 K (Fig. S4) do not exhibit saturation, consistent with the high anisotropy of these Ln^{III} and low-lying excited states.

8 exhibited a χ''_M versus T plot with only weak signals similar to **9**, but more encouraging results were observed for **5–7**, where the Ln^{III} ions bring both a large spin and large anisotropy to the molecules. Their $\chi'_M T$ versus T and χ''_M versus T plots are shown in Fig. 6, and two points should be noted: (a) in each case, the $\chi'_M T$ at 5.0 K is very similar to the corresponding dc $\chi_M T$ (Fig. 3) showing the latter not to be unduly affected by the dc field; and (b) in each case, below $\sim 3 \text{ K}$ there is a frequency-dependent drop in $\chi'_M T$ and a strong and frequency-dependent χ''_M peak, between one and two orders of magnitude larger than those in **4**. These data indicate **5–7** to possess significant relaxation barriers and thus be new SMMs.

The ac χ''_M versus T peak positions at different frequencies were used to obtain relaxation rate versus T data that were employed to

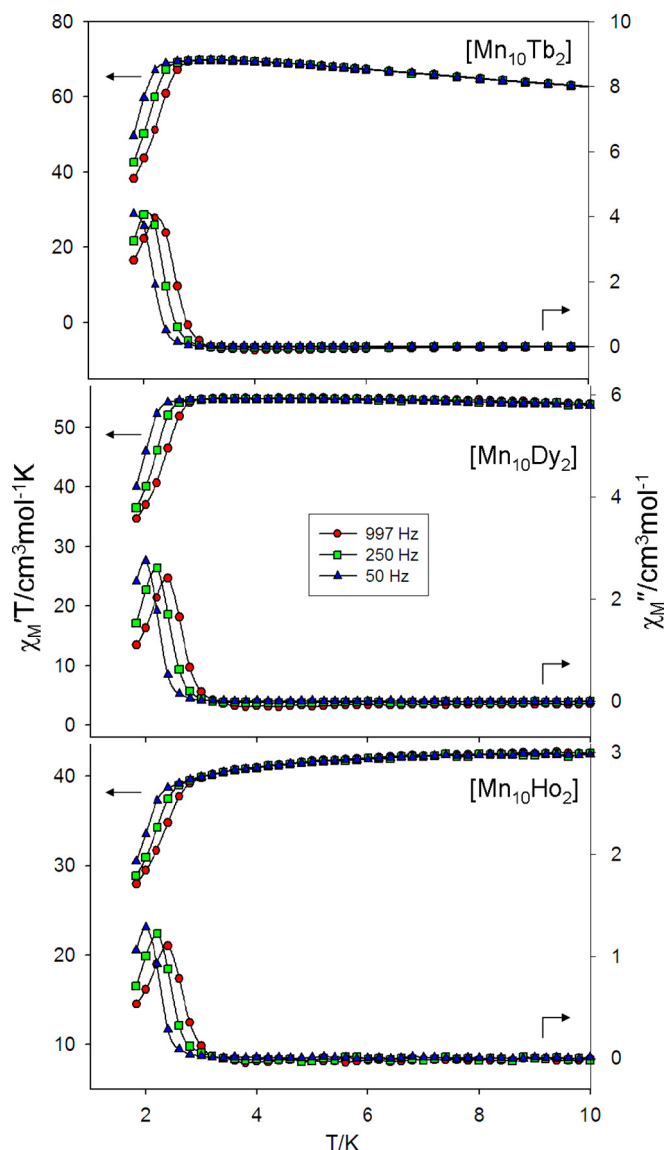


Fig. 6. Ac in-phase $\chi'_M T$ vs. T , and out-of-phase χ''_M vs T susceptibility plots for (top) **5**, (middle) **6**, and (bottom) **7** at the indicated frequencies.

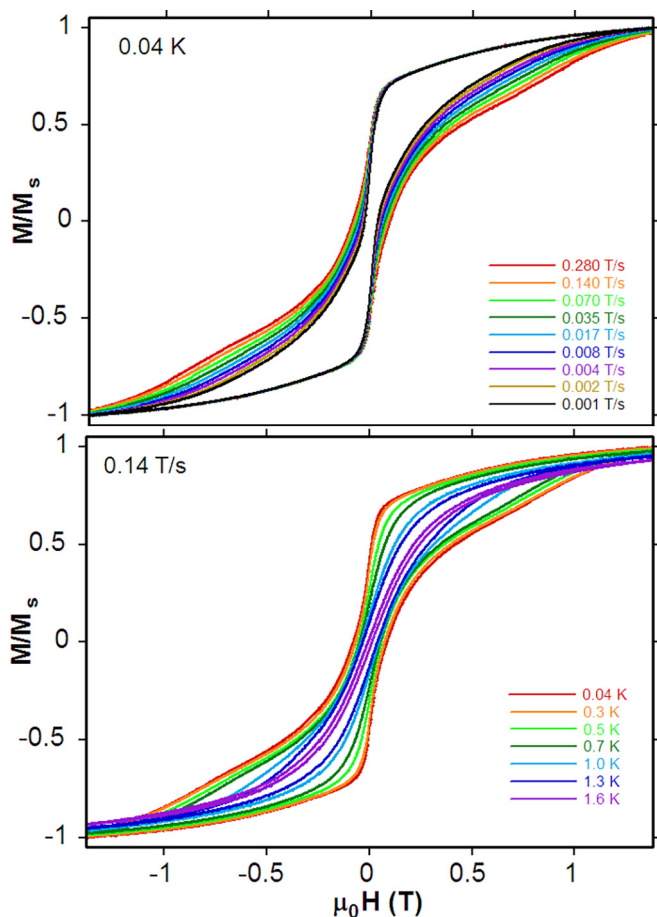


Fig. 7. Single-crystal magnetization (M) vs. dc field (H) hysteresis loops for a single crystal of **6**·3MeCN·MeOH at (top) different scan rates at 0.04 K, and (bottom) different temperatures at 0.14 T/s.

construct Arrhenius plots (Fig. S6), based on the Arrhenius Law of Eq. (3), where k is the Boltzmann constant and τ_0 is the pre-exponential factor. Fits of the data to

$$\tau = \tau_0 \exp(U_{\text{eff}}/kT) \quad (3)$$

Eq. (3) (solid lines in Fig. S6) gave the following for the effective barrier to magnetization relaxation (U_{eff}) and τ_0 : for **6**, $U_{\text{eff}} \sim 39$ K, $\tau_0 \sim 1 \times 10^{-11}$ s; for **7**, $U_{\text{eff}} \sim 41$ K, $\tau_0 \sim 3 \times 10^{-12}$ s. Because the ac χ''_M versus T data were over a small temperature range (~ 0.4 K), these values are only rough approximations. The χ''_M peaks for **5** were at lower T , giving even less data for a meaningful plot, but its U_{eff} was ~ 42 K.

3.4. Magnetization hysteresis loops

To confirm whether these complexes are truly SMMs, magnetization versus dc field sweeps were carried out using a micro-SQUID [33] on single crystals of representative complex **6**·3MeCN·MeOH. Hysteresis loops were observed below 1.6 K (Fig. 7), whose coercivity increases with decreasing T and increasing scan rate, as expected for an SMM. The loops are dominated by a large step at zero field due to quantum tunneling of magnetization (QTM) through the anisotropy barrier. The large step is indicative of fast QTM rates, as is typical for low symmetry molecules. Steps at other field positions are barely visible, and such smearing out is typical of broadening from effects such as low-lying excited states.

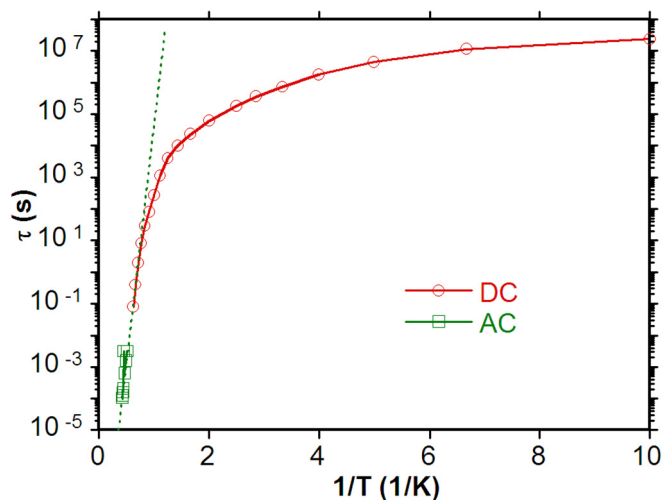


Fig. 8. Arrhenius plot of relaxation time (τ) vs. $1/T$ for **6** using combined ac χ''_M and dc magnetization decay data. The solid line is the fit to Eq. (3); see the text for the fit parameters.

A magnetization decay versus time study was carried out to obtain additional relaxation rate versus T data down to 0.04 K in order to obtain more accurate U_{eff} and τ_0 values for **6**. The magnetization of the crystal was saturated in one direction at ~ 5 K with a large applied dc field, the T was then decreased to a chosen value in the 0.04–1.6 K range, the field removed, and the magnetization monitored with time (Fig. S7). The fit in the thermally-activated region of the Arrhenius plot from the combined dc decay and ac χ''_M data (Fig. 8) gave $U_{\text{eff}} = 30$ K and $\tau_0 = 6 \times 10^{-10}$ s. Below ~ 1 K, the τ versus $1/T$ plot deviates from linearity as thermally-activated relaxation diminishes and the relaxation is dominated by QTM. Eventually at ~ 0.1 K, it becomes essentially temperature-independent, as expected for the relaxation now being exclusively by QTM. The latter was first observed for a 3d–4f complex in a $[\text{Mn}_{11}\text{Dy}_4]$ complex [19b]. The U_{eff} of 30 K is significantly lower than the 39 K obtained for **6** using just ac χ''_M data, and suggests those for **5** and **7** are also nearer 30 K than 40 K.

4. Conclusions

The reaction of a preformed Mn_4 cluster, hmpH and simple Ln^{III} salts has provided entry into a new family of 3d–4f $[\text{Ln}_2\text{Mn}_{10}]$ clusters. Three representative crystal structures have shown the complexes to be isostructural, including the corresponding $[\text{Y}_2\text{Mn}_{10}]$ analog with diamagnetic Y^{III} . Only the analogs containing Ln^{III} with high spin and large anisotropy, i.e., **5–7**, exhibit a significant relaxation barrier but even these are only moderate at best by modern standards. In fact, this is not surprising given that the Ln^{III} ions are at the ends of the molecule and attached to the Mn_{10} fragment by only one oxide and that one characteristic of this $\text{Ln}_2\text{Mn}_{10}$ family is that the coupling between the Ln ions and the central Mn_{10} subunits is not strong, even by typical 3d–4f standards. As a result, only at very low T does the molecule really behave as a single mixed-metal unit rather than almost independent Mn_{10} and Ln units. So at very low T , the anisotropy and spin of the Ln can couple with the Mn_{10} and give, for the Ln = Tb, Dy and Ho complexes, well observed χ''_M peaks indicating SMMs, confirmed for the Dy complex by the observation of hysteresis loops. However, the low-lying excited states prevent the relaxation continuing to be slow as the T is increased.

Acknowledgement

This work was supported by the National Science Foundation (CHE-1565664).

Appendix A. Supplementary data

CCDC 1565902, 1565903, and 1565904 contain the supplementary crystallographic data for **4**·3MeCN·MeOH, **6**·3MeCN·MeOH, and **9**·4MeCN, respectively. These data can be obtained free of charge via <http://www.ccdc.cam.ac.uk/conts/retrieving.html>, or from the Cambridge Crystallographic Data Centre, 12 Union Road, Cambridge CB2 1EZ, UK; fax: (+44) 1223-336-033; or e-mail: deposit@ccdc.cam.ac.uk. Supplementary data associated with this article can be found, in the online version, at <https://doi.org/10.1016/j.poly.2017.12.005>.

References

- [1] (a) R. Sessoli, D. Gatteschi, A. Caneschi, M. Novak, *Nature* 365 (1993) 141; (b) R. Sessoli, H. Tsai, A. Schake, S. Wang, J. Vincent, K. Folting, D. Gatteschi, G. Christou, D.J. Hendrickson, *J. Am. Chem. Soc.* 115 (1993) 1804.
- [2] (a) G. Christou, D. Gatteschi, D. Hendrickson, R. Sessoli, *MRS Bull.* 25 (2000) 66; (b) D.N. Hendrickson, G. Christou, H. Ishimoto, J. Yoo, E.K. Brechin, A. Yamaguchi, E.M. Rumberger, S.M.J. Aubin, Z.M. Sun, G. Aromi, *Polyhedron* 20 (2001) 1479.
- [3] D. Gatteschi, R. Sessoli, *Angew. Chem., Int. Ed.* 42 (2003) 268.
- [4] G. Aromi, E.K. Brechin, *Struct. Bonding* 122 (2006) 1.
- [5] H. Oshio, M. Nakano, *Chem. Eur. J.* 11 (2005) 5178.
- [6] (a) G. Christou, *Polyhedron* 24 (2005) 2065; (b) R. Bagai, G. Christou, *Chem. Soc. Rev.* 38 (2009) 1011.
- [7] (a) G.A. Craig, M. Murrie, *Chem. Soc. Rev.* 44 (2015) 2135; (b) Y.-S. Meng, S.-D. Jiang, B.-W. Wang, S. Gao, *Acc. Chem. Res.* 49 (2016) 2381.
- [8] D.N. Woodruff, R.E. Winpenny, R.A. Layfield, *Chem. Rev.* 113 (2013) 5110.
- [9] S.T. Liddle, J. van Slageren, *Chem. Soc. Rev.* 44 (2015) 6655.
- [10] (a) L.C. Pereira, C. Camp, J.T. Coutinho, L. Chatelain, P. Maldivi, M. Almeida, M. Mazzanti, *Inorg. Chem.* 53 (2014) (1811) 11809; (b) F. Moro, D.P. Mills, S.T. Liddle, J. van Slageren, *Angew. Chem., Int. Ed.* 52 (2013) 3430.
- [11] C. Papatriantafyllopoulou, E.E. Moushi, G. Christou, A.J. Tasiopoulos, *Chem. Soc. Rev.* 45 (2016) 1597.
- [12] L.M.C. Beltran, J.R. Long, *Acc. Chem. Res.* 38 (2005) 325.
- [13] R. Layfield, F.-S. Guo, B. Day, Y.-C. Chen, M.-L. Tong, A. Mansikamäkki, *Angew. Chem., Int. Ed.* (2017), <https://doi.org/10.1002/anie.201705426>, Accepted Author Manuscript.
- [14] (a) M.A. Bolcar, S.M.J. Aubin, K. Folting, D.N. Hendrickson, G. Christou, *J. Chem. Soc., Chem. Commun.* (1997) 1485; (b) C. Boskovic, E.K. Brechin, W.E. Streib, K. Folting, D.N. Hendrickson, G. Christou, *Chem. Commun.* (2001) 467; (c) A. Bhattacharjee, Y. Miyazaki, M. Nakano, J. Yoo, G. Christou, D.N. Hendrickson, M. Sorai, *Polyhedron* 20 (2001) 1607.
- [15] (a) E.K. Brechin, J. Yoo, M. Nakano, J.C. Huffman, D.N. Hendrickson, G. Christou, *Chem. Commun.* (1999) 783; (b) J. Yoo, E.K. Brechin, A. Yamaguchi, M. Nakano, J.C. Huffman, A.L. Maniero, L.-C. Brunel, K. Awaga, H. Ishimoto, G. Christou, D.N. Hendrickson, *Inorg. Chem.* 39 (2000) 3615; (c) C. Boskovic, E.K. Brechin, W.E. Streib, K. Folting, D.N. Hendrickson, G. Christou, *Chem. Commun.* (2001) 467.
- [16] (a) T. Taguchi, W. Wernsdorfer, K.A. Abboud, G. Christou, *Inorg. Chem.* 49 (2010) 199; (b) T. Taguchi, W. Wernsdorfer, K.A. Abboud, G. Christou, *Inorg. Chem.* 49 (2010) 10579.
- [17] T. Taguchi, M.R. Daniels, K.A. Abboud, G. Christou, *Inorg. Chem.* 48 (2009) 9325.
- [18] (a) S. Osa, T. Kido, N. Matsumoto, N. Re, A. Pochaba, J. Mrozinski, *J. Am. Chem. Soc.* 126 (2004) 420; (b) T. Hamamatsu, K. Yabe, M. Towatari, S. Osa, N. Matsumoto, N. Re, A. Pochaba, J. Mrozinski, J.L. Gallani, A. Barla, P. Imperia, C. Paulsen, J.P. Kappler, *Inorg. Chem.* 46 (2007) 4458; (c) J.P. Costes, M. Auchel, F. Dahan, V. Peyrou, S. Shova, W. Wernsdorfer, *Inorg. Chem.* 45 (2006) 1924.
- [19] (a) C.M. Zaleski, E.C. Depperman, J.W. Kampf, M.L. Kirk, V.L. Pecoraro, *Angew. Chem., Int. Ed.* 43 (2004) 3912; (b) A. Mishra, W. Wernsdorfer, K.A. Abboud, G. Christou, *J. Am. Chem. Soc.* 126 (2004) 15648; (c) A.J. Tasiopoulos, A. Mishra, G. Christou, *Polyhedron* 26 (2007) 2183.
- [20] (a) K. Liua, W. Shi, P. Cheng, *Coord. Chem. Rev.* 289–290 (2015) 74; (b) R. Sessoli, A.K. Powell, *Coord. Chem. Rev.* 253 (2009) 2328; (c) L.R. Piquer, E.C. Sañudo, *Dalton Trans.* 44 (2015) 8771.
- [21] (a) X.-J. Kong, Y.-P. Ren, W.-X. Chen, L.-S. Long, Z. Zheng, R.-B. Huang, L.-S. Zheng, *Chem. Commun.* (2008) 2398; (b) A.B. Canaj, D.A. Kalofolias, M. Siczek, T. Lis, R. McNab, G. Lorusso, R. Inglis, M. Evangelisti, C.J. Milios, *Dalton Trans.* 46 (2017) 3449.
- [22] (a) M. Murugesu, A. Mishra, W. Wernsdorfer, K.A. Abboud, G. Christou, *Polyhedron* 25 (2006) 613; (b) F. Mori, T. Nyui, T. Ishida, T. Nogami, K.Y. Choi, H. Nojiri, *J. Am. Chem. Soc.* 128 (2006) 1440.
- [23] M. Ferbinteanu, T. Kajiwara, K.Y. Choi, H. Nojiri, A. Nakamoto, N. Kojima, F. Cimpoesu, Y. Fujimura, S. Takaishi, M. Yamashita, *J. Am. Chem. Soc.* 128 (2006) 9008.
- [24] K.S. Pedersen, J. Bendix, R. Clérac, *Chem. Commun.* 50 (2014) 4396.
- [25] (a) C. Papatriantafyllopoulou, K.A. Abboud, G. Christou, *Inorg. Chem.* 50 (2011) 8959; (b) A. Mishra, A.J. Tasiopoulos, W. Wernsdorfer, K.A. Abboud, G. Christou, *Inorg. Chem.* 46 (2007) 3105; (c) C. Papatriantafyllopoulou, T.C. Stamatatos, C.G. Efthymiou, L. Cunha-Silva, F.A. Almeida-Paz, S.P. Perlepes, G. Christou, *Inorg. Chem.* 49 (2010) 9743.
- [26] J. Feuersenger, D. Prodius, V. Mereacre, R. Clérac, C.E. Anson, A.K. Powell, *Inorg. Chem. Commun.* 14 (2011) 1851.
- [27] C. Papatriantafyllopoulou, K.A. Abboud, G. Christou, *Polyhedron* 52 (2013) 196.
- [28] (a) L. Sun, H. Chen, C. Ma, C. Chen, *Dalton Trans.* 44 (2015) 20964; (b) L. Sun, H. Chen, C. Ma, C. Chen, *RSC Adv.* 6 (2016) 12408.
- [29] M.W. Wemple, H.L. Tsai, S.Y. Wang, J.P. Claude, W.E. Streib, J.C. Huffman, D.N. Hendrickson, G. Christou, *Inorg. Chem.* 35 (1996) 6437.
- [30] SHELXTL2014, Bruker-AXS, Madison, Wisconsin, USA, 2014.
- [31] P. van der Sluis, A.L. Spek, *Acta Crystallogr., Sect. A* 46 (1990) 194.
- [32] A.L. Spek, *Acta Crystallogr., Sect. D* 65 (2009) 148.
- [33] W. Wernsdorfer, *Adv. Chem. Phys.* 118 (2001) 99.
- [34] (a) E.C. Sanudo, E.K. Brechin, C. Boskovic, W. Wernsdorfer, J. Yoo, A. Yamaguchi, T.R. Concolino, K.A. Abboud, A.L. Rheingold, H. Ishimoto, D.N. Hendrickson, G. Christou, *Polyhedron* 22 (2003) 2267; (b) S. Wang, H.L. Tsai, K. Folting, W.E. Streib, D.N. Hendrickson, G. Christou, *Inorg. Chem.* 35 (1996) 7578.
- [35] (a) M. Shanmugam, G. Chastanet, T. Mallah, R. Sessoli, S.J. Teat, G.A. Timco, R.E. P. Winpenny, *Chem. Eur. J.* 12 (2006) 8777; (b) S. Maheswaran, G. Chastanet, S.J. Teat, T. Mallah, R. Sessoli, W. Wernsdorfer, R.E.P. Winpenny, *Angew. Chem., Int. Ed.* 44 (2005) 5044.
- [36] (a) A.M. Ako, V. Mereacre, I.J. Hewitt, R. Clerac, L. Lecren, C.E. Anson, A.K. Powell, *J. Mater. Chem.* 16 (2006) 2579; (b) E.K. Brechin, *Chem. Commun.* (2005) 5141.
- [37] L.M. Wittick, K.S. Murray, B. Moubaraki, S.R. Batten, L. Spiccia, K.J. Berry, *Dalton Trans.* (2004) 1003.
- [38] (a) A.J. Tasiopoulos, T.A. O'Brien, K.A. Abboud, G. Christou, *Angew. Chem., Int. Ed.* 43 (2004) 345; (b) A.J. Tasiopoulos, P.L. Milligan Jr, K.A. Abboud, T.A. O'Brien, G. Christou, *Inorg. Chem.* 46 (2007) 9678.
- [39] W.T. Liu, H.H. Thorp, *Inorg. Chem.* 32 (1993) 4102.
- [40] H.J. Eppley, S.M.J. Aubin, W.E. Streib, J.C. Bollinger, D.N. Hendrickson, G. Christou, *Inorg. Chem.* 36 (1997) 109.
- [41] V. Mereacre, D. Prodius, A.M. Ako, N. Kaur, J. Lipkowski, C. Simmons, N. Dalal, I. Geru, C.E. Anson, A.K. Powell, C. Turta, *Polyhedron* 27 (2008) 2459.
- [42] E.R. Davidson, *MAGNET*, Indiana University, Bloomington, IN, 1999.
- [43] E.R. Davidson, *GRID*, Indiana University, Bloomington, IN, 1999.
- [44] E.C. Sanudo, W. Wernsdorfer, K.A. Abboud, G. Christou, *Inorg. Chem.* 43 (2004) 4137.
- [45] C. Lampropoulos, T.C. Stamatatos, K.A. Abboud, G. Christou, *Inorg. Chem.* 48 (2009) 429.